

# A scalable, high-speed measurement-based quantum computer using trapped ions

René Stock<sup>1,\*</sup> and Daniel F. V. James<sup>1</sup>

<sup>1</sup>*Department of Physics, University of Toronto, Toronto, Ontario M5S 1A7, Canada*

(Dated: March 28, 2022)

We describe a scalable, high-speed, and robust architecture for measurement-based quantum-computing with trapped ions. Measurement-based quantum computing architectures offer a way to speed-up operation of a quantum computer significantly by parallelizing the slow entangling operations and transferring the speed requirement to fast measurement of qubits. We show that a 3D cluster state suitable for fault-tolerant quantum computing can be implemented on a 2D array of ion traps. We propose the projective measurement of ions via multi-photon photoionization for nanosecond measurement and operation and discuss the viability of such a scheme for Ca ions.

PACS numbers: 03.67.Lx, 03.67.Pp, 32.80.Fb

The rapid progress in quantum information processing systems has been fueled by the realization that the algorithmic complexity of a quantum computer scales polynomially with the size of certain important problems rather than exponentially [1]. This presents a tremendous advantage for large problems that are so far solvable only on a timescale of years. However, the practical utility of a large-scale quantum computers will also depend on their ability to compete with current classical computers on standard size problems. Consider, for example, Shor's factoring algorithm - an RSA640 number (640 bits) requires  $544 N^3$  two-qubit operations alone (neglecting error correction overheads) [2]. To compete with a distributed network that can factor a RSA640 number in 5 months [3], quantum operations on timescales of  $100\mu\text{s}$  are required. Moreover, to factor the same number on a quantum computer in 5s, operation timescales have to be improved to 2ns. *In other words, nanosecond timescale operations are an essential ingredient for practical large-scale quantum computers.*

In this article, we address this speed issue for one of the most promising quantum computing (QC) implementations, the ion-trap architecture [4]. In contrast to standard quantum circuit schemes considered so far for ion-traps, we consider measurement-based quantum computing paradigms [5], where the actual processor speed is mostly determined by the measurement time scales. We demonstrate i) that this one-way quantum computing (1WQC) scheme has significant advantages for ion-trap QC, ii) that a 3D cluster state for fault-tolerant computing can be efficiently implemented in a currently implementable 2D ion-trap architectures, and iii) that multi-photon ionization can significantly speed up measurement times for nanosecond operation.

Ions trap QC [4] has surpassed several major milestones on the QC roadmap [6]. Recent experiments have entangled up to eight ions [7, 8], demonstrated 99.3% fidelities for 21 successive entangling gates [9], coherence times of 10-34 seconds [10, 11], and high fidelity

single qubit operations [12]. Distant entanglement of ions via interference of emitted photon pairs has been demonstrated [13] and scalable trap architectures have been proposed for implementation of large scale quantum computation [14]. Also, much progress on chip-based ion-traps for such architectures has been made [15]. However, timescales for logic gate operations are slow, on the order of  $1\text{-}100\mu\text{s}$  for entangling gates [4, 16, 17] and  $1\mu\text{s}$  to 10ms for single qubit operations [12]. Moreover, the shuttling of ions required in scalable architectures puts even worse timing constraints on two qubit gates (about  $50\text{-}100\mu\text{s}$ ) [18]. Measurement-based quantum computing paradigms offers a way around this as the computational resource, a multipartite entangled state, can be created via entangling operation applied in parallel and offline [5]. This has the tremendous advantage that the usual requirement to avoid motional heating in ion traps is only restricted to this first entangling step and is removed from the actual QC process. In the 1WQC protocol, processing of information occurs through measuring different qubits in a prescribed basis and order combined with feedforward of measurement outcomes. The processor speed is then determined by the measurement, readout, and classical processing timescales which, as we will show, should be possible on a nanosecond timescale. Methods for error correction which introduce the necessity for 3D cluster states in one-way computing has recently been proposed [19]. We describe how this 3D cluster can be efficiently implemented in a 2D architecture.

In the one-way quantum computing paradigm, all entanglement operations are done in parallel and offline before commencement of the information processing. This multipartite entangled state, called a cluster state, is created via applying standard controlled phase (CPhase) gates [4, 16, 17] between neighboring atoms in a lattice geometry. In such a 2D array, measurements of the qubits in different bases and feedforward of measurement outcomes allows the simulation of a universal quantum circuit [5]. While this 2D cluster state represents a universal resource, so far only 3D structures have been shown to be suitable for error correction with high thresholds [19]. Topological encodings of the states in a 3D structure are necessary to protect the states against errors.

---

\*Electronic address: restock@physics.utoronto.ca

Due to the requirements of laser access, implementing a full 3D architecture for fault-tolerant 1WQC using ion traps would be extremely difficult. Instead, a 3D cluster state can be implemented efficiently in a 2D ion-trap array with non-nearest neighbor entanglement operations. The architecture required for implementing the one-way quantum computing paradigm is similar to the scalable ion-trap architectures proposed in [14]. This architecture requires inherently slow shuttling of ions between memory and interaction regions [18]. For faster transport, better fidelity and to keep ions in the motional ground state,  $120^\circ$  Y-junctions in a 2D hexagonal array (see Fig.1) are preferable to  $90^\circ$  junctions in a square lattice [15]. A cluster state with hexagonal structure, which would be created by employing connections between *all* sites, is a universal resource for quantum computation [20] but not suitable for error correction.

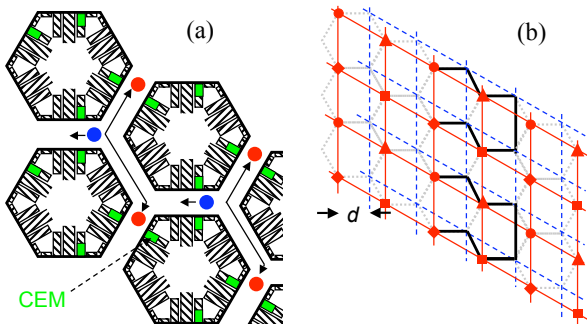


FIG. 1: (a) Hexagonal ion trap architecture with  $120^\circ$  junctions. (b) Underlying hexagonal array and resulting graph states for non-nearest neighbor interactions. The hexagonal array is decomposed into two rhombic lattices (red solid and blue dashed lines). Each lattice can again be broken down into further sublattices. For example, 4 sublattices of the solid line rhombic lattice are indicated by circles, squares, triangles and diamond. These, together with 4 sublattices of the dashed rhombic lattice can create an eight-layer 3D cluster state (see text for details). (Colour online.)

If we do not restrict ourselves to nearest neighbor entangling operation, then the hexagonal lattice can be broken down into two rhombic lattice sublattices with distance  $2d$  between sites as illustrated in Fig.1(b). Each of these two sublattices then represents a single 2D layer of a 3D cluster state. To create each layer of cluster state, atoms in each sublattice have to be entangled with its sublattice neighbors,  $2d$  away (Fig.1). This requires either shuttling of ions and moving one ion out of the way at a junction as illustrated in Fig.1(a) or swap operations between qubits at a junction to minimize movement of atoms. In each sublattice, a sequence of four parallel CPHASE gates entangles every ion with all four sublattice neighbors, creating a full 2D cluster state layer in the standard way [5]. Entanglement between different layers can be accomplished by simply entangling ions belonging to different sublattices selectively in just two parallel applications of a series of CPHASE gates as in-

dicated by thick black lines in Fig.1(b)]. The number of layers can be increased from 2 to  $2n^2$  by increasing the elementary cell of each sublattice by a factor  $n$ . This corresponds to entangling atoms separated by a distance  $2nd$  [see Fig.1(a)]. Note that the distance only scales as  $2n$  whereas the number of layers is  $2n^2$ . An example of an 8 layer system is shown in Fig.1(b) for a distance of  $4d$  between entangled atoms. Another important feature is the possibility to entangle the first and last layer of the 3D cluster state, thereby directly and efficiently creating a topological structure as required in [19]. In addition to standard entangling operation between nearby ions, probabilistic distant entangling operations [13] could be used to connect such 3D cluster states in separate location for building up a large scale 3D cluster state. The folding of a 3D cluster state into a 2D architecture is also of importance to other 1WQC candidates such as neutral-atom optical lattice systems and quantum dot systems where similar laser access restrictions apply.

Measurements of atomic qubits are usually achieved in two steps: Selection of basis, which corresponds to a single qubit rotation, followed by readout/projection into one of the two qubit states. Alkali-like ions such as Ca, Be, and Yb offer two different choices for encoding the two logical qubit states: The metastable  $S$ - $D$  transitions or encoding in the hyperfine structure of ions as shown in Fig.2. The choice of encoding has a consequence - the energy separation between states generally limits the possible single-qubit manipulation times due to energy-time uncertainty. First, for single qubit rotations, the light pulses that drive Raman transitions should have a bandwidth small compared to the energy separation. Second any readout pulse has to be able to resolve the two states. For example, a Fourier-limited pulse of 1 nanosecond duration has an energy-bandwidth of 1.5 GHz which is on the order of hyperfine splittings (3.25 GHz in  $^{43}\text{Ca}$ ). Polarization selective addressing of the qubit states may be possible for certain encodings but would not be applicable to the high-speed ionization readout scheme considered below.

For fast manipulation times an encoding in the optical  $S$ - $D$  transition would therefore be preferable. Transitions between the  $S$  ground state and metastable  $D$  state in Group II ions are electric-dipole forbidden and thus feature favorable long coherence times on the order of a second despite the optical energy separation of levels. To increase decoherence time further a mixture of encodings (e.g. in  $^{43}\text{Ca}$  [21]) would be conceivable, i.e. long-time storage in the hyperfine state and short-time storage in  $S$ - $D$  states for easier manipulation. To implement single qubit rotations on the  $S$ - $D$  transition, one can consider either allowed quadrupole transitions or two-photon Raman transitions using the intermediate  $P_{1/2}$  or  $P_{3/2}$  states (see Fig.2). The quadrupole transition Rabi frequencies can be obtained from the Einstein  $A_{SD}^{E2}$  coefficients (tabulated in [22]) via  $\Omega_{SD}^{E2} = eE_0/\hbar\sqrt{A_{SD}^{E2}/(4c\alpha k_{SD}^3)}$  [23]. Here,  $c$  is the speed of

light,  $\alpha$  the fine structure constant, and  $k_{SD} = 2\pi/\lambda_{SD}$  the wavevector for the transition. For Raman transition, we have  $\Omega_{SD}^{\text{Raman}} = \Omega_{SP}^{E1}\Omega_{PD}^{E1}/(2\Delta)$  with effective linewidth  $\gamma_{SD}^{\text{Raman}}$  and bare Rabi frequencies  $\Omega_{if}^{E1} = eE_0/\hbar \times \sqrt{A_{if}^{E1}/2c\alpha k_{if}^3}$  for the dipole allowed transitions. Quadrupole Rabi frequencies obtained in current experiments are on the order of 35.5 kHz for fairly low irradiance of about  $6\text{W}/\text{cm}^2$  (a few  $\mu\text{W}$  focused onto a spot with waist  $A = 2.5\mu\text{m}$ ) [12]. To achieve manipulations on a 2ns timescale (i.e.  $\Omega_{SD}^{E2} = (2\pi)5 \cdot 10^8\text{Hz}$ ) via quadrupole fields would require extremely high irradiances of  $10^9\text{W}/\text{cm}^2$ , which would lead to unwanted excitation due to off-resonant driving of electric dipole-allowed transitions. For faster single qubit rotation, we have to consider Raman transitions utilizing the P states instead. For example we can choose a detuning of  $\Delta/\Gamma_P = 10^{-4}$  to ensure low decoherence rates of the gate according to  $\gamma_{SD}^{\text{Raman}}/\Omega_{SD}^{\text{Raman}} \approx \Delta/\Gamma_P = 10^{-4}$ . In this case, to achieve manipulations on a 1ns timescale, irradiance of  $10^5\text{W}/\text{cm}^2$  is sufficient, which corresponds to a 5mW beam focused onto a spot with waist  $A = 2.5\mu\text{m}$ .

A more severe timing limit is due to the fluorescence readout in ion systems where one of the two qubit states is coupled to a shelving state via a cycling transition [12]. The timescales for this are limited by the lifetimes of dipole transitions and photo collections and detection efficiencies to a few microseconds. However nanosecond projective measurements via state-dependent multiphoton ionization and subsequent detection of the freed electron allow detection on nanosecond timescales. For a concrete example consider a resonant four-photon ionization of  $\text{Ca}^+$  in the  $S$ -state. A schematic of the possible ionization paths is shown in Fig. 2. The ionization energy required to remove the second electron of Ca is 11.87 eV. As excitation wavelengths, we consider easily accessible 380 – 410nm ( $\approx 3.1$  eV). From the level diagram in Fig.2, it is immediately apparent that a multiphoton ionization transition should be possible for fairly low intensities. For 380 – 410nm, the four photon transition is close to resonance with several levels. We can choose a resonance condition for the  $4P_{1/2}$  state at 397nm, the  $5S_{1/2}$  state at 383nm, or the  $6P_{1/2}$  and  $6P_{3/2}$  states at 403nm. On the other hand photoionization of the  $D$ -level is strongly suppressed, as the detunings are an order of magnitude larger for each transition. A broadband frequency doubled Ti:Sapphire would be able to address all three wavelengths. Using appropriate pulse shaping one would be able to exploit constructive and destructive interference between the different ionization paths to improve the ionization fidelity and state discrimination.

Using the effective operator method in [24], the resonant ionization probability for the  $S$ -state for  $\pi$  polarization is  $N_{\pi}^S = \sum_{E_{\lambda}} 4\pi I^4 (J_{\pi}^{\lambda})^2 + 4\pi I^2 K^2/L^2$ , where the non-resonant contributions are described by  $J_{\pi}^{\lambda}$  for transitions to the different possible continua  $E_{\lambda} = E_s, E_d, E_g,$  and  $E_i$  [24]. The resonant  $L, K$  transition operators are also given in [24]. For the non-resonant  $D$ -state ion-

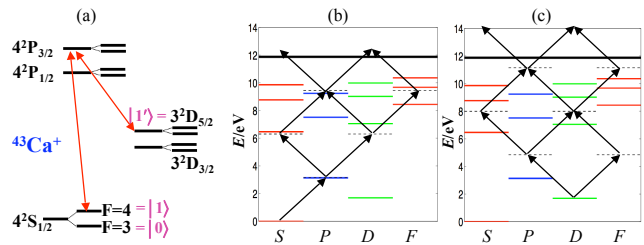


FIG. 2: (a) Ground state levels of  $^{43}\text{Ca}^+$ . Quantum information can be encoded either in the hyperfine structure as  $|0\rangle$  and  $|1\rangle$ , or for faster manipulation in the  $S$ - $D$  transition as  $|0\rangle$  and  $|1'\rangle$ . Relevant levels for ionization-readout scheme of the (b)  $S$ -state and (c)  $D$ -state. Contributing transitions are shown with black arrows. (Colour online.)

ization, we only have an incoherent sum of the transition rates,  $N_{\pi}^D = \sum_{E_{\lambda}} 4\pi (J_{\pi}^{\lambda})^2 I^4$ . We include only dominant, near-resonance transitions in our estimate of the ionization rates, which can be found in [22] (non-listed matrix elements have been estimated by simple scaling arguments). Using this basic estimate, we expect the non-resonant parts of photoionization probability to be a factor of at least  $[(J_{\pi}^{\lambda})_S/(J_{\pi}^{\lambda})_D]^2 = 1600$  lower for atoms in the  $D$  state compared to the  $S$  state. This difference allows a very high fidelity state discrimination as would be necessary for a projective measurement. At resonance with the  $6P_{1/2}$  state, we expect ionization rates on the order of  $N_{\pi}^S \approx 10^9 - 10^{10}\text{s}^{-1}$  for peak intensities of about  $10^9\text{W}/\text{cm}^2$ . This allows for a fast ionization on a femtosecond or picosecond timescale with accessible laser intensities (see also optimal-control femtosecond ionization experiments in atomic Ca [25]).

Photoionization and detection of ions has been used in multiple experiments, e.g. for high fidelity counting of atoms [26], imaging of a gas of atoms [27] and even single atoms in a cloud [28]. It has been proposed for fast readout of logic states in neutral atoms [29]. Detection of electrons via a single channel electron multiplier (CEM) is generally more efficient at above 99% efficiency than detection of the heavy ion [30]. A CEM also features detector deadtimes of nanoseconds or less [30]. Not only is the detection probability higher for the freed electron compared to the ion, but the electron mobility is higher, suitable for fast detection. Furthermore, the electron is not trapped by the dynamic trapping potential as the characteristic parameter  $q_x^e \propto \sqrt{e/m_e}$  is two orders of magnitude too large compared to the one for the ion  $q_x^{\text{ion}} \propto \sqrt{e/m_{\text{ion}}} \approx 0.5$ ;  $\omega_{\text{rf}}$  for ion-trap field is typically on the order of 20-30 MHz [12]. The characteristic timescale for the electron motion  $t_0 = \sqrt{R_0^2 m_e / V_0 q} \approx 1/\omega_{\text{rf}} \sqrt{m_e/m_{\text{ion}}}$  in the ion trap is about 0.5ns. The field is therefore time-independent on the electron detection timescale. If we assume all momentum from the four photon ionization is transferred to the electron, since the effective mass of the trapped ion approaches infinity, the corresponding initial electron velocity is  $7 \cdot 10^3\text{m/s}$ . We assume that

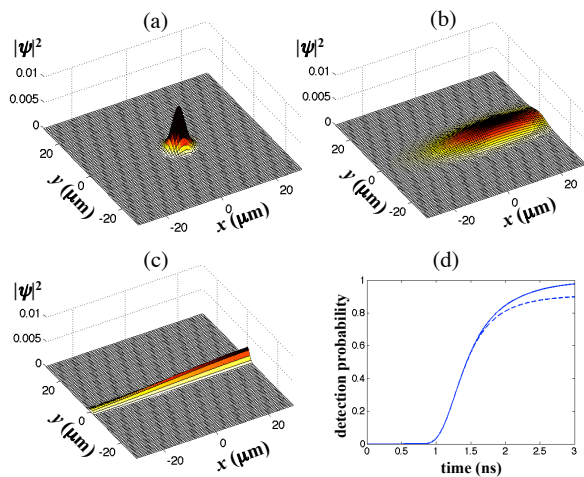


FIG. 3: (a-c) Time evolution of the emitted electron in the ion-trap saddle potential at three different times, (a) 0.25 ns (b) 1.0 ns (c) 1.5 ns. We assume an initial kick of the electrons in the positive  $x$ -direction. (d) If we place one detector about  $30\mu\text{m}$  away on the  $x$ -axis, we can detect the electron with up to 90% fidelity [see dashed line in (d)]. A second detector can be placed on the negative  $x$ -axis to detect the part of the wave packet that escaped along the saddle in this direction. The detection efficiency is then above 99% within a 3ns time window [solid line in (d)]. (Colour online.)

the electron is ejected when the dynamic trap potential is anti-trapping in the  $x$ -direction and trapping in the  $y$ -direction (with a static weak trap field in the longitudinal  $z$ -direction as in [12]). For simplicity, the laser beam is also oriented along the  $x$ -axis, even though access may be restricted in practice. A full time-dependent simulation of the electron wavepacket dynamics shows that we can reach close to 99% efficiency within 3 nanoseconds (see Fig.2).

The wave packet simulation in Fig.3 shows that the electron remains localized in the  $y$ -direction with the typical wave packet breathing due to squeezing in the  $y$ -direction. In the  $x$ -direction, the electron wave packet

“slides” slowly down the saddle of the trapping potential due to the initial momentum kick of the four photoionization photons. If we place two  $20\mu\text{m}$  size CEM detector about  $30\mu\text{m}$  away from the trap center close to the trap-electrodes on the positive and negative  $x$ -axis, we can estimate above 99% detection efficiency within 3ns [Fig.3(d)]. Due to trap geometry, placement of detectors may be restricted, but the initial conditions (direction of photoionization beam, timing of ionization) should make it possible to guide the electron into the detector using the existing trap-field.

For above ionization readout, we also need to consider what happens to the remaining doubly ionized  $\text{Ca}^{++}$  atom. The trap-parameters  $q_x \propto \sqrt{q/m}$  can be chosen carefully so that both  $\text{Ca}^+$  and  $\text{Ca}^{++}$  are trapped in a stable regime. This can be accomplished as  $q_x$  only changes by a factor of  $\sqrt{2}$  from  $\text{Ca}^+$  to  $\text{Ca}^{++}$ . In reality, practical constraints such minimization of micro-motion [12], may dictate parameters that would result in the loss of the doubly charged ion. The relevant timescale for the ion to become unstable in the trap is slower than  $1/\omega_{\text{rf}}$  ( $0.1\text{-}1\mu\text{s}$ ). The measurement time is much shorter and qubit readout for the one-way quantum computing process will have moved on to other qubits, 10-100 qubits farther away, so that measurements are not affected. Finally, each ion is located in separate regions of the architecture (several  $100\mu\text{m}$  apart) and coupling to other ions can be neglected. Thus any DC stark shifts or Debye-Waller shifts of the Rabi frequencies can be neglected as well. The one draw back is that the trap would have to be reloaded before running another algorithm.

Our results certainly indicate that measurement-based quantum computing with nanosecond measurement times presents a extremely promising solution to the speed constraints in quantum computing. A detailed experimental analysis is needed to determine realistic error rates, and more theoretical work is on it way to determine accurate error correction thresholds and overheads.

We thank S. Ghose for helpful discussions and suggestions for improving the manuscript. This work was supported by NSERC and ARO.

- 
- [1] M. A. Nielsen and I. L. Chuang, *Quantum computation and information* (University Press, Cambridge, 2000).  
[2] R. J. Hughes *et al.*, Phys. Rev. Lett. **77**, 3240 (1996).  
[3] www.rsasecurity.com.  
[4] J. I. Cirac and P. Zoller, Phys. Rev. Lett. **74**, 4091 (1995).  
[5] R. Raussendorf, D. E. Browne, and H.-J. Briegel, Phys. Rev. A **68**, 022312 (2003).  
[6] R. Hughes *et al.*, A Quantum Information Science and Technology Roadmap. [http://qist.lanl.gov/pdfs/rm\\_intro.pdf](http://qist.lanl.gov/pdfs/rm_intro.pdf) (2004).  
[7] H. Häffner *et al.*, Nature **438**, 643 (2005).  
[8] D. Leibfried *et al.*, Nature **438**, 639 (2005).  
[9] J. Benhelm *et al.*, Nat. Phys. **4**, 463 (2008).  
[10] C. Langer *et al.*, Phys. Rev. Lett. **95**, 060502 (2005).  
[11] H. Häffner *et al.*, Appl. Phys. B **81**, 151 (2005).  
[12] F. Schmidt-Kaler *et al.*, Appl. Phys. B **77**, 789 (2003).  
[13] D. L. Moehring *et al.*, Nature **449**, 68 (2007).  
[14] D. Kielpinski, C. Monroe, and D. J. Wineland, Nature **417**, 709 (2002).  
[15] Kim *et al.*, Quantum Inf. Comput. **5**, 515 (2005). R. Slusher, private communication (2008).  
[16] A. Sorensen and K. Molmer, Phys. Rev. Lett. **82**, 1971 (1999).  
[17] J. J. Garcia-Ripoll, P. Zoller, and J. I. Cirac, Phys. Rev. Lett. **91**, 157901 (2003).  
[18] D. Hucul *et al.*, Quant. Inf. Comp. **8**, 0501 (2008).  
[19] R. Raussendorf and J. Harrington, Phys. Rev. Lett. **98**, 190504 (2007).

- [20] M. Van den Nest *et al.*, *New J. Phys.* **9**, 204 (2007).
- [21] J. Benhelm *et al.*, *Phys. Rev. A* **77**, 062306 (2008).
- [22] Y. Ralchenko *et al.*, NIST Atomic Spectra Database v. 3.1.5. <http://physics.nist.gov/asd3>.
- [23] D. F. V. James, *Appl. Phys. B* **66**, 181 (1998).
- [24] M. Crance, *J. Phys. B* **11**, 1931 (1978).
- [25] E. Papastathopoulos, M. Strehle, and G. Gerber, *Chem. Phys. Lett.* **408**, 65 (2005).
- [26] T. Campey *et al.*, *Phys. Rev. A* **74**, 043612 (2006).
- [27] A. Robert *et al.*, *Science* **292**, 461 (2001).
- [28] T. Gericke *et al.*, arXiv:0804.4788 (2008).
- [29] R. Stock *et al.*, *Phys. Rev. A* **78**, 022301 (2008).
- [30] M. P. Seah, *J. Electron. Spectrosc.* **50**, 137 (1990).